Maturation and rejuvenation of a silicic magma reservoir: High-resolution chronology of the Kneeling Nun Tuff

Journal Article

Author(s):
Szymanowski, Dawid; Ellis, Ben S.; Wotzlaw, Jörn-Frederik; Bachmann, Olivier

Publication date:
2019-03-15

Permanent link:
https://doi.org/10.3929/ethz-b-000322342

Originally published in:
Earth and Planetary Science Letters 510, https://doi.org/10.1016/j.epsl.2019.01.007

Funding acknowledgement:
155923 - Taking apart a 'super' eruption: the Kneeling Nun Tuff, New Mexico (SNF)

*Manuscript

Maturation and rejuvenation of a silicic magma reservoir: high-resolution chronology of the Kneeling Nun Tuff

Dawid Szymanowski, Ben S. Ellis, Jörn-Frederik Wotzlaw, Olivier Bachmann

Institute of Geochemistry and Petrology, Department of Earth Sciences, ETH Zürich, Clausiusstrasse 25, 8092 Zürich, Switzerland; dawid.szymanowski@erdw.ethz.ch

Abstract

Knowledge of the conditions of magma storage prior to volcanic eruptions is key to their forecasting, yet little is known about how melt compositions, crystallinity and intensive parameters within individual magma reservoirs evolve over time. To address this, we studied the Kneeling Nun Tuff, a voluminous (>900 km^3) deposit of an Eocene caldera-forming eruption from the Mogollon–Datil volcanic field in New Mexico, USA. Whole-rock, feldspar and amphibole compositions were combined with zircon trace-element geochemistry and precise isotope dilution–thermal ionisation mass spectrometry (ID–TIMS) U–Pb zircon crystallisation ages to arrive at a detailed, time-resolved record of chemical and physical changes within the voluminous, upper-crustal (~2.2 kbar) magma reservoir. Chemical compositions and zircon ages of the Kneeling Nun Tuff and co-magmatic clasts hosted within it reveal prolonged (>1.5 million years) growth and maturation of the magma reservoir that was heterogeneous in terms of temperature, melt composition and crystallinity. This protracted storage at a dominant crystallinity in excess of 50% culminated in a period of ca. 50 ky of increase in recharge heat supply and related homogenisation, decrease in crystallinity to 40–50%, and potential increase in average melt temperature, leading up to eruption at 35.299 ± 0.039 Ma. Sampling of co-magmatic lithic clasts derived from early-cooled domains of the reservoir show that the long, million year-scale maturation time is shared across all erupted domains of the magmatic system, irrespective of their final cooling history. This study provides key observations from a natural system against which thermal and mechanical models of upper-crustal magma reservoir construction can be validated.

1. Introduction

Explosive volcanic eruptions can have tremendous effects on both the Earth system and society, ranging from local-scale devastation to global perturbations of the climate system caused by release of volcanic gases (Self, 2006). Understanding how magma bodies feeding such eruptions work, as well as achieving the long-term goal of forecasting eruptions, crucially depends on the knowledge of the mode of magma storage (e.g. crystallinity, temperature, pressure, volatile content, all affecting its physical properties) and the timescale of the system's maturation prior to eruption. The physical state of a magma reservoir is key in the context of detecting such bodies by geophysical methods in the present day as well as reading their readiness to erupt (e.g. Flinders et al., 2018; Kiser et al., 2018). In turn, the temporal aspect of magma residence feeds into a better understanding of magmatic fluxes, eruption frequencies and magnitudes (Costa, 2008). It is particularly important to know how magma parameters vary over time, e.g. whether the baseline (dormancy) magma storage conditions need to be drastically altered in a lead-up to an eruption, as proposed for silicic, high-crystallinity systems (Bachmann and Bergantz, 2003). Therefore, our understanding of upper-crustal magmatic processes would benefit from a detailed, absolute chronology of physical and chemical fluctuations in a fossil magma reservoir. Such a record has the potential to bring new insights about the magnitude, character and duration of key events in a magmatic system's life.

Ideally, such a chronology could be extracted from the most abundant, major mineral phases such as feldspar, pyroxene or quartz. However, the often-detailed stratigraphy of events preserved as compositional zoning in these phases carries little information that can be placed in absolute time. Given the relatively fast diffusion of most major and trace elements in these phases at magmatic temperatures (often utilised to constrain diffusion timescales; Costa et al., 2008), the compositions of the measured crystals will represent partial equilibration i.e. the conditions of crystallisation modified by any subsequent diffusion. Using independent estimates of the temperature of storage of a crystal, diffusion modelling can then be used to constrain the maximum amount of time spent in magma at given conditions (Cooper and Kent, 2014). This approach is capable of delivering important insights about the thermal history of individual crystals since a given (e.g. rim) crystallisation event, but currently cannot constrain the age of crystallisation itself. The only absolute, high-temperature chronometer for major phases applicable to this problem relies on U-series disequilibria and requires analysing large separates of minerals from young rocks, which results in complex averaging effects (Cooper, 2015). As a consequence, building a reliable chronology of pre-eruptive events using the most abundant and sensitive, major mineral phases remains challenging.

An alternative is to focus on zircon, a common accessory phase in silicic igneous rocks. Due to extremely slow diffusion of most trace elements (Cherniak and Watson, 2003), zircon crystals faithfully record melt composition and changes in intensive parameters while allowing them to be placed in a temporal framework using the U–Pb chronometer. Such approaches have been used for young magmatic rocks mostly in the ^{230}Th–^{238}U disequilibrium range (Vazquez and Reid, 2004; Stelten et al., 2013; Barboni et al., 2016; Tierney et al., 2016; Kaiser et al., 2017) but it has been shown that in some cases the interpretations may be non-unique primarily due to poor precision of individual zircon ages when compared to the expected duration of the events (Kent and Cooper, 2017). While *in situ* ^{230}Th–^{238}U dating is the method of choice for magmatic systems younger than ca. 400,000 years, the majority of the most voluminous eruptions in the geological record and all known plutons are significantly older, requiring alternative analytical approaches. For such cases, zircon geochronology by isotope dilution–thermal ionisation mass spectrometry (ID-TIMS) has been shown to provide sufficient precision (typical single-crystal date uncertainties of <1 ‰) to resolve the timescales of magmatic processes on the scale of a single magma body (e.g. Coleman et al., 2004; Schaltegger et al., 2009). In particular, the combination of this technique with either bulk-grain or *in situ* zircon chemical and isotopic information can yield time–composition systematics useful in constraining large-scale changes of magmatic conditions (Schoene et al., 2012; Wotzlaw et al., 2013; Rivera et al., 2014; Samperton et al., 2015).

Here we present a case study employing high-precision zircon U–Pb dating by ID-TIMS to construct a detailed pre-eruptive chronology of events in a large magmatic system. We studied the Kneeling Nun Tuff, a voluminous (> 900 km^3) deposit of an Eocene super-eruption fed by a long-lived magmatic reservoir (Szymanowski et al., 2017) with both traditional tools of petrology and detailed zircon petrochronology, allowing new insights into the maturation and rejuvenation of magmas feeding such large-volume caldera-forming eruptions.

2. Kneeling Nun Tuff

The Kneeling Nun Tuff (KNT) is a voluminous ignimbrite emplaced within the Mogollon–Datil volcanic field (MDVF) in western New Mexico, USA (Fig. 1; McIntosh et al., 1990; McIntosh et al., 1992; Chapin et al., 2004). The MDVF is part of a discontinuous belt of mid-Tertiary silicic volcanic fields extending from the southern Rocky Mountains in Colorado in the north (Lipman, 2007) to Sierra Madre Occidental in central Mexico in the south (McDowell and McIntosh, 2012; Fig. 1a). The Mid-Tertiary volcanic activity in this area was mostly characterised by an arc-like geochemical signature (high-K calc-alkaline series) related to the subduction of the Farallon plate beneath North America, however the large distance from the plate margin in present Colorado and New Mexico would require this subduction to be of low angle (Lipman et al., 1972; Coney and Reynolds, 1977). Alternatively, interpretations involving magma generation from the sub-continental lithospheric mantle previously modified by subduction have been proposed (Davis and Hawkesworth, 1993; Farmer et al., 2007).

MDVF activity followed a pattern similar to other Tertiary volcanic fields of SW North America, where early intermediate volcanism was followed by voluminous caldera-forming eruptions of silicic magma (cf. Lipman, 2007). In the MDVF, initial andesitic volcanism dominated between 40–36 Ma before episodic bimodal basaltic andesite–silicic activity became predominant between 36–24 Ma (Elston, 1984; McIntosh et al., 1990; McIntosh et al., 1992). The Kneeling Nun Tuff (Elston, 1957) was erupted from the Emory caldera (Elston et al., 1975) in the southern part of the Black Range at the SE edge of MDVF (Fig. 1b) at 35.36 ± 0.05 Ma (recalculated from McIntosh et al., 1990) and is considered the largest eruption of the first pulse of MDVF silicic volcanism (McIntosh et al., 1992).

The Kneeling Nun Tuff occurs both in thick intracaldera facies (500–1000 m; Kuellmer, 1954; Elston et al., 1975) and outflow facies (up to 150 m thick) extending at least 30 km beyond the caldera margins (Fig. 1b). This extent led to a minimum eruptive volume estimate of 900 km^3 (Elston et al., 1975) placing the KNT among the largest silicic eruptions in the geological record (Mason et al., 2004). The KNT outflow typically forms conspicuous, columnar-jointed red cliffs of welded ignimbrite (Fig. 2a), which are often subdivided by local breaks into multiple 'cooling units' reflecting the complex nature of pyroclastic density currents and effects of variable topography (e.g. Giles, 1965). The KNT typically overlies a thick sequence of broadly andesitic lavas and tuffs of the Rubio Peak formation, but locally a sequence of rhyolitic ignimbrites and air fall tuffs mapped as the Sugarlump Formation occurs beneath the KNT (Elston, 1957). Dated at 35.64 ± 0.12 Ma (recalculated from McIntosh et al., 1990), some of the Sugarlump tuffs may represent precursor eruptions from the same magmatic system that fed the KNT.

The Kneeling Nun Tuff is a crystal-rich (trachy)dacite to rhyolite carrying a mineral assemblage of quartz + sanidine + plagioclase + biotite + hornblende + rare clinopyroxene + magnetite + ilmenite + titanite + apatite + zircon. The reported crystal content is between 25 and 60% (Giles, 1965). The KNT outflow sheets are locally zoned, with an upward increase in crystallinity, phenocryst size and the proportion of plagioclase and ferromagnesian phases accompanied by a decrease in the amount of quartz and alkali feldspar (Giles, 1968). Both outflow and intracaldera KNT facies contain abundant crystal-rich pumice, rare crystal-poor pumice and xenoliths of underlying Rubio Peak andesites, Palaeozoic basement rocks, and granites, porphyries and aplites of variable texture which may be partly contemporaneous and genetically related to KNT magma (Elston, 1989). Abundant cm-sized xenoliths are present throughout the ignimbrite but in some areas within the caldera they become larger (up to tens of metres) and form zones of 'megabreccia' that were previously interpreted as vent or collapse breccias (Kuellmer, 1954; Elston, 1989).

3. Samples

A total of 26 samples of different facies of the Kneeling Nun Tuff have been studied, comprising two main groups:

1) Samples of bulk KNT ignimbrite from the SW (Lucky Bill Canyon) and E (Tierra Blanca) outflow sheets as well as the caldera fill (Fig. 1), ranging from early- to late-erupted material. Detailed studies of the two outflow sections (Table 1; Supplementary Fig. 2) are complemented by samples used only for bulk chemical analyses (Supplementary Tables 1, 2).

2) A suite of magmatic clasts of presumed cogenetic character found within both intracaldera and outflow facies of the ignimbrite (Table 1, Fig. 1). The samples were

assigned to one of three groups: i) pumices, which have clear indications of ductile behaviour upon deposition (ubiquitous flattening, Fig. 2b), ii) porphyries, containing large phenocrysts in a formerly glassy matrix, but without clear evidence of syn-depositional deformation (Fig. 2d, e), and iii) plutonic lithics—angular fragments of holocrystalline, porphyritic to equigranular granites (Fig. 2c, f).

4. Analytical Methods

The samples were characterised by a combination of bulk chemical analyses, major element chemistry of main rock-forming mineral phases (feldspars, amphibole) and *in situ* trace element analyses of accessory zircon, followed by high-precision U–Pb isotope analyses of the same, partly polished down, zircon crystals.

Whole-rock compositions were determined following standard procedures by X-ray fluorescence (XRF) of fused glass beads with complementary laser ablation–inductively coupled plasma mass spectrometry (LA-ICPMS) analyses of trace elements. Feldspar and amphibole major elements were analysed in thin sections by electron probe microanalysis (EPMA). A subset of feldspar crystals was also analysed for trace elements by LA-ICPMS.

In order to obtain a time-resolved record of the KNT magma storage regime, a particular focus was placed upon studying the textures, compositions and crystallisation ages of zircon crystals separated from magmatic clasts found within the ignimbrite. The analytical approach taken here is identical to that presented by Szymanowski et al. (2017), which allows a direct comparison of zircons separated from a bulk ignimbrite sample with those hosted by the various types of clasts. First, the zircons were mounted in epoxy, polished and imaged using cathodoluminescence (CL), which was followed by *in situ* analyses by LA-ICPMS for trace elements and U–Pb isotopes to screen out inherited cores. Particular care was taken to ensure the accuracy of Ti analyses, which was made possible by the introduction of the Ti-rich zircon reference material GZ7 (Szymanowski et al., 2018). Based on zircon compositions determined *in situ* and their CL textures, some crystals were selected for extraction from the epoxy mounts for dissolution and high-precision U–Pb analyses by chemical abrasion (CA)–isotope dilution–thermal ionisation mass spectrometry (ID-TIMS).

A complete description of all analytical procedures as well as tables with sample coordinates and all analytical data are provided as Supplementary Material.

5. Results

5.1. Whole-rock compositions and crystallinity

Bulk samples of KNT ignimbrite range in composition from (trachy-)dacite to rhyolite (67–77 wt% SiO_2, Supplementary Fig. 1 and Table 1) with crystallinities of 32–58% (11% in the basal fallout). Of the two outflow sections studied in detail (Fig. 1), one (Lucky Bill Canyon; samples 1519–1523) displays clear, systematic variations from early-erupted, evolved (>70 wt% SiO_2), less crystalline material to crystal-rich (46–55%), (trachy-)dacitic (67–69 wt% SiO_2), late-erupted material towards the top of the section (Supplementary Fig. 2). The other section (Tierra Blanca; samples 1428–1435) does not show any substantial variability in compositions, but the earliest-erupted material is similarly crystal-poor. Key major and trace elements are characteristically correlated with SiO_2 (Supplementary Fig. 1), and their trends are indicative of fractionation of feldspars, hornblende, Fe–Ti oxides, titanite, zircon and apatite, consistent with the observed mineral assemblage. The variability between early-erupted and late-erupted compositions can therefore be fully explained in terms of variable melt extraction and crystal accumulation within the upper-crustal magma reservoir. All sampled KNT-hosted clasts define the same compositional array (Supplementary Fig. 1), with the bulk compositions corresponding to their mineral assemblage and crystallinity.

5.2. Feldspars

Feldspar occurs in the KNT as fragments of mostly euhedral plagioclase and sanidine that show little major element variability within individual crystals, samples, between parts of the deposit, or within the juvenile/lithic clasts (Table 1; Supplementary Figs 3, 4). Plagioclase ranges mostly between An_{20} and An_{28} with rare cores of up to An_{51}, presumably inherited from deeper differentiation steps. An contents lower than ~20 are present exclusively in early-erupted material (samples 1519–1521, 1428), the crystal-poor pumice (1434) and the plutonic lithics (1421, 1510). Sanidine displays similarly little variability in major elements (Table 1; Supplementary Figs 3, 4); typical compositions are $Or_{61–66}$, with notable exceptions of elevated K in the porphyritic samples (1416A, 1509A, 1511; $Or_{64–69}$) and the basal fallout (1519, $Or_{69–71}$). Corresponding two-feldspar pairs reveal equilibrium temperatures (Putirka, 2008) of ~730–820 °C for most late-erupted material, crystal-rich pumice and porphyritic clasts, while the crystal-poor pumice, all early-erupted material and plutonic lithologies return lower temperatures ranging from ~760 °C down to 640 °C (in the basal fallout; Table 1, Supplementary Fig. 2).

An additional feature of KNT sanidine is the common occurrence of one or more growth rims, present either as simple growth zones or surrounding a resorbed core, that are enriched in Ba (Fig. 3). The rims occur in most late-erupted parts of the ignimbrite as well as the porphyritic clasts, but are seemingly lacking in early-erupted and evolved-composition samples (Table 1). Their BaO contents are up to 2 wt% (Supplementary Table 3); representative trace element data (Fig. 3) show that increased Ba is accompanied by enrichments in elements compatible in the bulk mineral assemblage such as Sr, Ti, P and REE and depletions in the incompatible Rb. Additionally, Pb-isotopic compositions of these rims tend to be somewhat less radiogenic than the respective cores (Szymanowski et al., 2017).

5.3. Amphibole

Except for rare (n=5) cores of tschermakitic composition, all of the analysed amphibole crystals across bulk ignimbrite, pumice and porphyritic clast samples (n=115) are Mg-hornblendes with a very restricted compositional range and no clear zoning within individual crystals (Supplementary Table 4). The dominant, homogeneous population of hornblende satisfies criteria for equilibrium with the corresponding plagioclase at temperatures between 700–810 °C (Holland and Blundy, 1994), consistent with two-feldspar thermometry (Table 1) as well as the results of zircon- and titanite-based thermometry (Szymanowski et al., 2017). Given the low-variance, near-solidus mineral assemblage of KNT, we applied the revised Al-in-hornblende geobarometer of Mutch et al. (2016), which yields a uniform pressure estimate of 2.22 ± 0.10 kbar (1σ) for the equilibrium hornblendes. The rare higher Al tschermakitic cores crystallised at pressures of 3–4 kbar and are interpreted as representing deeper stages of differentiation of magmas feeding the shallow KNT reservoir.

5.4. Zircon

5.4.1. Textures

Zircon crystals from the bulk KNT ignimbrite and the clasts hosted within it are typically euhedral and prismatic irrespective of the sample lithology (Fig. 4). Nearly all grains display complex oscillatory (and rare sector) zoning testifying to their complex crystallisation histories. A subset of zircons, found in samples 1402, 1525-2 and 1509A, is characterised by large size (up to >500 μm length), simple zonation patterns and conspicuously high CL intensities (Fig. 4) correlating to low rare earth element (REE) contents (section 5.4.3).

5.4.2. High-precision U–Pb geochronology

ID-TIMS U–Pb dating was performed on single zircons extracted from three kinds of magmatic clasts; pumices (2 samples), porphyries (3 samples), and plutonic lithics (2 samples; Fig. 5). The targeted crystals were pre-screened for inherited cores and inclusions based on CL imaging and *in situ* chemical analyses and except for one dated zircon (1416A z21) did not show any indication of inheritance. With the exception of one of the plutonic clasts (1510-1) which is distinctly older than the remaining samples, the ranges of individual zircon dates from each clast overlap to a large degree both between samples and with the bulk outflow ignimbrite zircons analysed previously by Szymanowski et al. (2017). This supports field relationships between the clasts and the hosting Kneeling Nun Tuff and confirms that all overlapping samples, and likely also the granitic clast 1510-1, are sourced from the same upper-crustal magmatic system. The re-sampling of this system additionally confirms its longevity, with the zircon from clast samples spanning ranges of U–Pb dates from 341 ± 20 ky to as much as 1.22 ± 0.14 My, broadly comparable to 618 ± 56 ky obtained for the bulk ignimbrite.

The Kneeling Nun Tuff eruption age can now be defined as either the Th-corrected $^{206}Pb/^{238}U$ date of the single youngest zircon (35.305 ± 0.021/0.024/0.045 Ma) or a Bayesian estimate (Keller et al., 2018) using a bootstrapped prior distribution based on data from juvenile samples, yielding 35.299 ± 0.039/0.040/0.056 Ma (2σ uncertainty given as internal only/with tracer calibration/with ^{238}U decay constant). The two estimates are indistinguishable and both are fully consistent with the existing $^{40}Ar/^{39}Ar$ sanidine dates of the KNT (McIntosh et al., 1990) recalculated to the more recent standard and decay constant calibration of Kuiper et al. (2008; Fig. 5). The $^{40}Ar/^{39}Ar$ age of the uppermost Sugarlump tuffs (McIntosh et al., 1990) overlaps with most of the zircon crystallisation interval, suggesting a genetic relationship between at least some of the Sugarlump eruptions and the KNT.

Individual dates of zircons from both pumice samples (the evolved, high-Si 1434A, and the low-Si 1525-2) range from ones close to, or overlapping, eruption age at 35.299 ± 0.039 Ma and up to a maximum of 36.077 ± 0.023 Ma (Fig. 5). While the number of analysed zircons is smaller (n=8) and consequently the sampled populations are less representative than the large bulk ignimbrite dataset, the pumices preserve an indistinguishable age distribution, suggesting that they sample a comparable age domain. In contrast to the pumices, the textures of the porphyries imply rapid cooling of these magma volumes some time before eruption. This appears true for all three porphyry samples as they record the same time of peak zircon crystallisation and apparent pre-eruptive gaps in zircon distributions of 67 ± 49, 134 ± 42 and 291 ± 45 ky. However, one exception is that sample 1509A contains one young zircon with a date overlapping the eruption age. The plutonic samples, consistently with textures requiring slow cooling pre-dating the eruption, only contain zircons with crystallisation ages significantly older than the eruption age. The granitic clast 1421, similarly to porphyry samples, records zircon crystallisation coeval with that found in pumices and in bulk ignimbrite, but with a pre-eruptive gap of 168 ± 41 ky. Clast 1510-1 represents an early period of intrusion with zircon crystallisation ages from 36.896 ± 0.082 to 36.653 ± 0.025 Ma. These granitic clasts show that during most of the time of magma reservoir assembly, portions of the reservoir were fully solid, forming ‘cool’ wall-rock around the active, eruptible domains.

5.4.3. Trace elements

Trace elements in KNT zircons (Fig. 6, Supplementary Figs 5, 6) show large variability consistent with the complex CL textures and the complexity expected from sampling domains of the magmatic system with different thermal histories. The zircon compositions testify to the key control exerted by co-crystallising titanite and, to a lesser degree, hornblende over REE budgets, which can be shown with simple geochemical models (Szymanowski et al., 2017) for both REE contents and heavy/middle REE ratios (e.g. Yb/Dy). Strong correlations exist between titanite indicators (e.g. MREE or Th/U) and the temperature-dependent Ti contents (Ferry and Watson, 2007). This is particularly the case for low-Ti zircons, suggesting relatively low-T titanite saturation. Zr-in-titanite thermometry (Szymanowski et al., 2017), recalculated to the amphibole pressure of 2.2 kbar, places titanite saturation for KNT at around 734 °C.

Combining trace elements with bulk-grain crystallisation ages (Fig. 6) reveals a complex history of zircon crystallisation within the KNT magma reservoir. While individual samples do not provide sufficient data points to evaluate any temporal trends, all data taken together reveal important reservoir-scale systematics. For most of the reservoir's lifetime, the zircons are characterised by significant compositional scatter with dominant low-T, evolved compositions (e.g. Eu/Eu* of 0.2–0.5, Ti: 3-10 ppm, Dy <200 ppm) punctuated by analyses indicating both higher temperature (high Ti), less-evolved melts (e.g. high Eu/Eu*, Dy, low Yb/Dy) and lower temperature, more-evolved melt compositions (low Ti, Eu/Eu*, Dy, high Yb/Dy). The sense of measured zonation within individual crystals is highly variable, with inner zones ('cores' in Supplementary Figs 5, 6) generally showing more scatter than rim compositions. However, the CL-bright, texturally simple crystals (Fig. 4) with bulk U–Pb ages between ~35.35 Ma and eruption age at 35.299 Ma exhibit a striking compositional focussing trend towards increased Eu/Eu* (0.3–0.7), Ti (6–19 ppm) and variably decreased REE (e.g. Dy <150 ppm, Yb <500 ppm), Yb/Dy (<6) (Fig. 6). The observation of this compositional trend across three separate samples suggests a critical change in magmatic storage conditions that affected large portions of the magma reservoir in the last ~50 ky before eruption.

6. Discussion

6.1. Magmatic architecture and storage conditions determined from major mineral phases

Compositions of major mineral phases in the Kneeling Nun Tuff constrain the dominant magma storage conditions to a pressure of ~2.2 kbar (ca. 7–9 km depth) and temperatures between ~670 °C and 820 °C (Table 1), consistent with its near-solidus mineral assemblage. Pre-eruptive crystallinity of the dominant volume of erupted magma (as documented in the late-erupted samples) appears to have been on the order of 40–50%, but locally or episodically reached values in excess of 60% (Table 1). Such high crystallinity may imply rheological lock-up in the form of a rigid crystal mush, which facilitates the long-term survival of the magma body but requires a process eventually reducing the crystal content for most of the reservoir volume to erupt (Marsh, 1981; Bachmann et al., 2002; Bachmann and Bergantz, 2003). Locally melts would get extracted from the mush zone, creating pools of more evolved, crystal-poor material, represented by crystal-poor pumice (1434), the basal fallout (1519) and, as variable mixtures with crystal-rich material, in early-erupted magma (Table 1).

Amphibole and feldspar compositions, as well as those of bulk rock (Supplementary Fig. 1), reveal large-scale compositional homogeneity of the KNT magma reservoir. Most of the variability in whole-rock compositions is attributable to variable mineral proportions and crystallinity, while all deviations in feldspar major element compositions and temperatures (Table 1) could result from either 1) local melt extraction or 2) variable cooling of different domains sampled by clasts. In particular, the lowest An contents of plagioclase are associated with extracted melts either in the evolved pumice (1434), in all early-erupted material, or in the slowly-cooled plutonic clasts (Supplementary Fig. 4).

Similarly, all deviations to higher orthoclase contents of K-feldspars occur either in extracted melts (1519) or in porphyry samples which presumably did not readjust their compositions to predominant pre-eruptive conditions due to ‘premature’ solidification.

The occurrence of high-Ba rims in sanidine (Fig. 3) requires the episodic presence of melts enriched, with respect to background values of melt in equilibrium with most of sanidine volume, in Ba and other bulk-compatible elements (Section 5.2). Such compositions can generally be expected as a result of either 1) recharge of the system with less evolved melts, or 2) melting of the resident mush in response to a heat and volatile addition, with the melting phase assemblage dictating the elemental enrichments (Wolff et al., 2015; Forni et al., 2016). In the KNT, the enrichments would require the melting of cumulate sanidine + plagioclase (Ba, Sr), titanite (Ti, REE) and apatite (P), most likely accompanied by quartz and biotite as low-temperature phases. The wide range of published partition coefficients for trace elements in sanidine are permissive of very large enrichments even at equilibrium, precluding a unique interpretation; additionally, it is doubtful that such cumulate-derived crystallisation reflects at all an equilibrium process (e.g. Arzilli et al., 2018). In reality the generation of any cumulate melt is likely caused by an influx of hotter recharge magma, so the two processes should be expected to act together. In the KNT, the presence of ubiquitous, often multi-stage high-Ba rims in the crystal-rich, late-erupted material as well as in the porphyry samples (which presumably cooled down before eruption) suggest that recharge and cumulate melting are common and repeated processes. This is in line with the long-lived nature of the KNT system, which requires a persistent influx of heat delivered through recharge magma to remain thermally buffered over timescales of several hundred thousand years (Szymanowski et al., 2017).

While the major mineral phases provide a relatively simple view of magmatic storage in the KNT reservoir, it is crucial to emphasise which 'time slice' of the prolonged, million-year history of the magmatic system they represent. For feldspar and amphibole (or any other magmatic mineral), the compositions of erupted crystals should represent conditions at time of crystallisation modified by any subsequent diffusion. In these two minerals, the retention of most major and trace elements at magmatic conditions is relatively limited, and depends primarily on their post-crystallisation storage history (Cooper and Kent, 2014). If storage temperatures can be estimated independently, one can model the storage time of individual crystals since a given (e.g. high-Ba rim) crystallisation event, but this result remains relative to the assumptions made. For that reason, in the following sections we focus on zircon petrochronology which can be used to obtain a more faithful, time-resolved record of magma reservoir evolution.

6.2. *Time-resolved record of magmatic storage and rejuvenation*

Zircon trace element compositions can be interpreted in terms of changes in both melt composition and intensive parameters such as temperature (Melnik and Bindeman, 2018). Given the comparable timescales of zircon growth and diffusive equilibration (Watson, 1996; Cherniak and Watson, 2003), except for sector zones, zircon compositions are expected to faithfully record the chemical and physical environment at time of growth. Consequently, with an understanding of the main factors controlling zircon chemistry, both the temporal and the compositional information in zircon may be exploited to construct a chronology of major pre-eruptive events in a magmatic system (e.g. Wotzlaw et al., 2013; Barboni et al., 2016). In many cases, particularly for young rocks, the analytical age resolution may not be adequate to resolve events with sufficient certainty (Kent and Cooper, 2017). In the case presented here for the Kneeling Nun Tuff, the precision afforded by applying ID-TIMS dating (2σ uncertainties on individual dates 11–

177 ka) theoretically provides a chance to describe such systematics with highly precise constraints in the time dimension. The main challenge of our approach lies in matching *in situ* measured compositions with bulk-crystal U–Pb ages (Fig. 6). We chose to assign compositional data to the age constraint of the respective sectioned crystal fragment, which may to some extent obscure reservoir-scale systematics (if they exist) and mask small-scale secular compositional variations for all but the youngest crystals. Crucially, zircon crystals of age close to eruption are least likely to contain a significantly older inner zone biasing the bulk-crystal age, so all of their trace element compositions, including those of cores, can be considered robust. Even given the limitations of this approach, the large dataset of such (variably biased) zircon composition–age pairs allows us to draw first-order conclusions about the character, magnitude, and duration of magma reservoir-wide processes, with a particular focus on the youngest, pre-eruptive events.

Figure 6 illustrates that in the KNT magma, and presumably in other long-lived magmatic systems that experience recurring recharge, multiple physical conditions/melt compositions can be present at any given time. In other words, the degree of magmatic evolution, e.g. along a liquid line of descent, does not equate to time (cf. simply cooling magmatic systems, e.g. Samperton et al., 2015). Instead, trace elements in KNT zircon show that environments of varying temperature, crystallinity, or mineral proportions (e.g. samples of cumulate character vs. extracted melts) can coexist and can ultimately be sampled by the same eruption (Fig. 6, Supplementary Fig. 5, 6). The key trace element trajectories depicted in Fig. 6 all show large variability in zircon compositions for most of the system's lifetime, ranging from those corresponding to low-crystallinity, relatively unevolved melts to some indicating highly fractionated, crystalline environments (mostly innermost cores, Supplementary Fig. 6). However, after ~35.35 Ma, or ~50 ky prior to eruption, the system appears to undergo a significant change exhibited in more focussed, or systematically offset, compositions. The negative Eu anomaly (Eu/Eu*), primarily controlled by crystallisation/melting of feldspar, records a notable shallowing towards the eruption (Fig. 6a). At the same time, Dy and Yb/Dy, both controlled by titanite crystallisation (i.e. in a titanite-saturated system, its crystallinity), record a shift towards titanite undersaturation (Fig. 6c, d). The increase in the temperature-dependent Ti towards the eruption may reflect an increase in melt temperature, assuming activities of Ti and Si in the melt remain constant (Ferry and Watson, 2007). Alternatively, influx of less evolved melts and the associated (non-modal?) melting of minerals may alter both the Ti and Si activity in a way that is difficult to predict or model, which could result in both completely masking (higher a_{TiO2} or lower a_{SiO2}) and strengthening (lower a_{TiO2}) the potential signal of temperature increase.

To understand better the nature of the melts represented by the measured zircon compositions, we modelled melts in equilibrium with all KNT zircons using a temperature-dependent parametrisation of zircon–melt element partitioning that uses Ti-in-zircon as a temperature proxy (Claiborne et al., 2018). This approximation, while potentially strongly biased by the accuracy of Ti quantification, proves useful in simulating the first-order control of temperature on partitioning (Fig. 7). Assuming that differences in Ti represent real temperature variations, we inverted zircon trace element compositions (Fig. 7a) to their corresponding melts (Fig. 7b). This resulted in melt compositions that are broadly consistent with the KNT bulk rock trend, and display a remarkable transition between relatively hot, titanite-undersaturated melts (low Yb/Dy, high Dy in Fig. 7b) and relatively cold, near-solidus, titanite-saturated melts (high Yb/Dy, low Dy). In the KNT, where REEs are almost exclusively controlled by titanite (Szymanowski et al., 2017), trends towards melts with high Yb/Dy can be explained only by co-crystallising titanite, while the reverse (to low Yb/Dy, high Dy) can be accomplished by both mixing with less evolved melts and melting of pre-existing titanite. At the same time, changes in Eu/Eu* (Fig. 6a) result in an identical interpretation for feldspar crystallisation and melting. As a consequence, zircon compositions alone are unable to discriminate between an influx of recharge melts and the melting of cumulates caused by the heat delivered by the same process (Wolff et al., 2015).

Plotting the resulting melt compositions against time (Fig. 8) creates a record of highly diverse conditions for most of the magma reservoir's lifetime, varying between hot, titanite-undersaturated and, more commonly, near-solidus, titanite-saturated (< 734 °C) melts. This is consistent with previous results for KNT implying magma storage dominantly within the titanite crystallisation window (Szymanowski et al., 2017) as well as thermal models (Gelman et al., 2013; Karakas et al., 2017) suggesting that maintaining upper-crustal silicic magma reservoirs for 10^5–10^6 years is favoured for high-crystallinity, near-solidus bodies that receive their heat through episodic magma recharge (here likely represented by 'hot', high-REE, high-Eu/Eu* melts). We interpret the last ~50 ky to represent a period of increased recharge heat and mass supply which resulted in decrease in crystallinity, increase in temperature and gradual homogenisation of the magma reservoir in the lead-up to eruption (Fig. 9). Similar mechanisms have been invoked as means of rejuvenating evolved magmatic systems from their baseline, high-crystallinity state to an intermediate-crystallinity state that is rheologically mobile and eruptible, with modelled timescales between months to years (Burgisser and Bergantz, 2011) to 10^3–10^5 years (Bachmann and Bergantz, 2003; Huber et al., 2012). Other studies using zircon geochronology have inferred timescales of ~200 ky for the 5000 km^3 Fish Canyon Tuff (Wotzlaw et al., 2013), ~10 ky for the 1000 km^3 Lava Creek Tuff (Matthews et al., 2015), ~15–40 ky for smaller eruptions at Soufrière, St. Lucia (Barboni et al., 2016). Here we show that for the >900 km^3 Kneeling Nun Tuff, rejuvenation took on the order of 50 ky, which adds to the growing database of such well-described eruptive units.

6.3. Coeval environments of variable cooling history

Studying clasts erupted together with the KNT ignimbrite allows us to evaluate not only the homogeneity of the system in major and trace element compositions (section 6.1) but also its temporal evolution across multiple 'facies' of the magmatic source. The fact that there is no clear distinction in the mineral compositions between these clasts (Supplementary Fig. 4), as well as the great overlap in zircon dates (Fig. 5) and trace elements (Fig. 6), show that all these lithologies are sampled from the same, voluminous, long-lived (> 1 My) upper-crustal magma reservoir. However, the textures of the clasts (Fig. 2) suggest different scenarios for their final cooling and solidification, ranging from slow cooling for the holocrystalline, plutonic samples, to rapid but sub-surface freezing of the porphyritic clasts and syn-eruptive quenching of the pumices. The textural information is aided by zircon age distributions (Fig. 5), creating a fingerprint of the thermal history of individual magma volumes in the context of the entire magma reservoir (Fig. 9). The plutonic clasts likely represent peripheral volumes of the system; we speculate that at some point of its maturation, insufficient heat is supplied from the recharging magma to keep the particular magma portion above solidus, resulting in slow cooling and formation of the plutonic rind (effectively the wall rock) of the system. Porphyritic clasts require rapid freezing, which may be a result of decompression, e.g. related to previous eruptions (such as the Sugarlump tuffs), or ascent and emplacement in much cooler surroundings. Long apparent hiatuses in zircon crystallisation (such as 280 ky in porphyritic clast 1509A; Fig. 5) suggest locally or episodically slowed growth rates or zircon undersaturation and resorption; however, they do not require extended subsolidus storage. Finally, pumices represent batches of magma that was mobile at eruption (Fig. 9). Irrespective of the complexity of individual cooling paths of the clasts, the reproducibility of the age spectrum of the bulk ignimbrite sample in the clast-hosted zircons (Fig. 5) suggests that every sample may capture essentially the entire life of the KNT magmatic system from early intrusions to solidification/eruption.

6.4. Zircon age distributions and the estimation of eruption ages

Dating past eruptions is an invaluable component of many studies requiring independent information about the timing of events in the geological past. Indeed, ID-TIMS U–Pb dating of zircon from distal volcanic ash beds intercalated with sedimentary sequences has played a key role in the establishment of the absolute time framework of the geologic timescale (Gradstein et al., 2012). Understanding magmatic zircon age distributions and developing accurate ways of estimating the eruption age from a population of volcanic zircon (see e.g. Schmitz and Davydov, 2011; Schoene et al., 2015; Keller et al., 2018 for interpretation strategies) is therefore critical to progress in resolving the rates of geological processes. The large (n=76) set of ID-TIMS dates generated here from a proximal deposit of a super-eruption (Fig. 5) can be considered a suitable proxy for the true distribution of zircon crystallisation ages in upper-crustal magma bodies (albeit one truncated at eruption).

A key observation that can be made for KNT zircon is that their distribution in time (and temperature; Figs 5, 6) differs from distributions predicted by theoretical considerations or observed in simple plutonic systems (Watson, 1996; Samperton et al., 2017; Keller et al., 2018). In particular, the main apparent peak of zircon crystallisation occurs relatively late in the total lifetime of the system, some 100–300 ky before the eruption (Fig. 5). While our dataset might to some extent be biased by high U contents (pulling the grain-average ages towards times of crystallisation from high-crystallinity, evolved magma), it should be expected that incrementally built magma reservoirs characterised by protracted growth and storage have a history involving multiple transitions between zircon-saturated and undersaturated conditions. Consequently, models proposing a simple relationship between temperature, time and zircon saturation (Samperton et al., 2017) can only work for the simplest of systems such as monotonously cooled, single magma batches. We expect the products of most (at least wet, calc-alkaline) explosive volcanic eruptions of all but the smallest size to have complex zircon age spectra such as that shown here for KNT.

In cases where the total timescale of zircon crystallisation is much greater than analytical uncertainty (such as the KNT), both youngest-zircon and Bayesian modelling approaches to eruption age estimation can be expected to give indistinguishable and accurate results for all reasonable zircon numbers (n > ca. 10–15) (Keller et al., 2018). However, strategies for estimating eruption ages of many other, particularly ash bed, samples (other n, absolute age, analytical uncertainty, age dispersion) might benefit from directed rather than random sampling, e.g. using additional textural and compositional information from the available zircons. Our data show that KNT zircons younger than ~35.35 Ma, i.e. those interpreted to represent the rejuvenation interval, are distinct both texturally (large, CL-bright, simple zoning; Fig. 4) and compositionally (low REE, high Eu/Eu*, Ti; Fig. 6). If such systematics are widespread in explosive volcanic units, then age interpretations can be substantially improved by careful characterisation of ash bed zircons with either *in situ* or bulk analyses (Schoene et al., 2010; Schoene et al., 2015; Wotzlaw et al., 2018). Gathering compositional information from zircons from out-of-context or altered airfall ash beds (bentonites, tonsteins etc.) can have the additional benefit of establishing the tectonic affinity of the source of volcanism (e.g. Grimes et al., 2015), which should further improve the age interpretations as age dispersion may be systematically different for within-plate and subduction volcanism.

7. Conclusions

Zircon age and trace element data presented here for the Kneeling Nun magmatic system provide a detailed record of magma chamber maturation and rejuvenation in the build-up to one of the largest eruptions in the geological record. This unique, large dataset for a single eruption reveals long and complex storage of magma in the form of a high crystallinity mush, dominantly at near-solidus temperatures (< ca. 730 °C), but large internal temperature and crystallinity variations as a function of location with respect to the heat source. We show that the prolonged accumulation, storage and maturation of KNT magmas of at least 1.5 million years culminated in a period of ~50 ky of increase in heat supply and related homogenisation, decrease in crystallinity, reversal in the degree of melt evolution and, potentially, increase in average melt temperature. The decrease in crystallinity in particular may have conditioned the magmatic system for the cataclysmic eruption by driving it from rheologically immobile to mobile conditions; however, with our data we cannot address the ultimate eruption trigger. The insights gained from the zircon record, aided by estimates of magma storage conditions from major mineral phases, make the Kneeling Nun Tuff an extraordinary subject to develop new ways of studying the pre-eruptive history of magmas.

Acknowledgements

This research was supported by Swiss National Science Foundation grant 200021_155923. We thank F. Forni for detailed discussions, M. Guillong for help with laser ablation analyses, and D. Klimentyeva, G. Ligęza, L. Zehnder and M. Castellanos for help with sample characterisation. We are also grateful to C. Klemp and K. Cook from Freeport-McMoRan Inc. for facilitating access to outcrops near Chino Mine, New Mexico. We thank K. Cooper and an anonymous reviewer for insightful comments which helped us improve the manuscript.

Figure captions

Fig. 1. Location of the study area and Kneeling Nun Tuff sampling sites. (**a**) Map of the distribution of Tertiary volcanic rocks in SW North America (modified from McDowell and McIntosh, 2012); SJ–San Juan/Southern Rocky Mountain volcanic field; MD–Mogollon–Datil; BH–Boot Heel; TP–Trans-Pecos; SMO–Sierra Madre Occidental; GB–Great Basin. (**b**) Location of the Emory caldera, source of the Kneeling Nun Tuff, within the Mogollon–Datil volcanic field in western New Mexico, with the approximate extent of the KNT ignimbrite sheet proposed by McIntosh et al. (1992) based on paleomagnetic and $^{40}Ar/^{39}Ar$ data of distal samples. Three key areas were targeted for sampling: western outflow sheet at Lucky Bill Canyon, Hurley and inside Chino Mine; intracaldera KNT along NM-152 west of Emory Pass; eastern outflow sheet immediately south of Tierra Blanca valley.

Fig. 2. Field appearance and microscopic textures of studied lithologies. (**a**) The eruptive unit's namesake, the Kneeling Nun landmark near Santa Rita, NM. (**b–f**) Field appearance of studied clasts including crystal-rich pumice (**b**), plutonic clasts (**c,f**) and porphyries (**d,e**). The field scale in **d** is marked every 1 cm. (**g–j**) Cross-polarised light thin section images of representative samples of a porphyry (1509A, **g**), a crystal-rich pumice (1525-2, **h**), an evolved, quartz-rich pumice (1434, **i**) and a holocrystalline granitic clast (1421, **j**).

Fig. 3. Trace element (Ba, Sr) compositions of representative KNT sanidine, illustrating the magnitude of variations in compatible elements. Inset: a backscattered electron image of a sanidine crystal typical for late-erupted material (Table 1) with a prominent, high-Ba rim.

Fig. 4. Cathodoluminescence (CL) images of representative Kneeling Nun Tuff zircon crystals from samples 1402, 1416, 1509A, 1511, and 1525-2. Note the frequent truncations and complex zonation patterns. The white frame highlights CL-bright, simply zoned, REE-depleted crystals with $^{206}Pb/^{238}U$ dates between 35.352 and 35.305 Ma.

Fig. 5. Texturally resolved geochronology of the Kneeling Nun magmatic system. Coloured bars represent Th-corrected ID-TIMS $^{206}Pb/^{238}U$ dates of individual zircon crystals together with their 2σ uncertainty. Bulk-ignimbrite zircon and titanite data for sample 1402 is reproduced from Szymanowski et al. (2017). $^{40}Ar/^{39}Ar$ sanidine dates for KNT and uppermost Sugarlump tuffs (McIntosh et al., 1990) were recalculated to the calibration of Kuiper et al. (2008). The preferred eruption age is the Bayesian estimate following Keller et al. (2018) displayed with three uncertainty envelopes: internal only/with tracer calibration/with tracer and ^{238}U decay constant. Side panel: colour-coded kernel density plots illustrating the zircon age distribution of individual samples and a histogram of all zircon dates in this study.

Fig. 6. Variability of selected trace elements in Kneeling Nun Tuff zircon through time. Each point represents one *in situ* LA-ICPMS analysis prior to ID-TIMS U–Pb dating of the bulk crystal; in cases where multiple spot analyses of a crystal are available, they are assigned the same crystallisation age. Note that the real crystallisation ages of the sampled spots may deviate from the assigned ones as bulk U–Pb dates are likely to be biased towards ages of rims and high-U zones. Box plots show medians, interquartile ranges (IR), and extreme values for bins of 50 ky (7 youngest bins) or more (dates > 35.655 Ma). T-tests for Eu/Eu* (a) and Ti (b) reveal that compositions of zircon in the youngest bin (50 ky prior to eruption, grey shaded area) are statistically distinct from the compositions of older crystals at high significance level ($p < 0.01$). These younger crystals further show significantly lower variance with respect to Dy and Yb/Dy. Typical

uncertainties are based on counting statistics for element ratios (Yb/Dy, Eu/Eu*) or counting statistics and the composition of primary reference materials for Ti and Dy. For Dy the error bar is smaller than symbol size. Ti was either analysed relative to reference zircon GZ7 (Szymanowski et al., 2018) for clast-hosted zircon or recalculated to match the same calibration (via zircon 91500) for previously analysed zircon from bulk sample 1402. Ti-in-zircon temperature estimates use the model of Ferry and Watson (2007) and assume same activity values as in Szymanowski et al. (2017).

Fig. 7. Trace elements in zircon and their corresponding melts, colour-coded for Ti content in zircon. (**a**) Results of LA-ICPMS measurements of KNT zircon across all dated samples. (**b**) Melts in equilibrium with individual measured zircon compositions, calculated using power-law fits between Ti and zircon–melt partition coefficients (Claiborne et al., 2018). Titanite saturation temperature is the average Zr-in-titanite temperature of Szymanowski et al. (2017) adjusted for pressure of 2.2 kbar.

Fig. 8. Composition of reconstructed Kneeling Nun Tuff melts through time. Each point corresponds to a datum in Fig. 6. The time coordinate is identical to that of the corresponding whole-zircon crystallisation age, while the composition is recalculated from the respective *in situ* zircon analysis using the model of Claiborne et al. (2018) as in Fig. 7. In cases of multiple compositions assigned to the same age, the points are connected with a vertical line.

Fig. 9. Conceptual model of the storage and remobilisation of the Kneeling Nun magmatic system. (**a–b**) Two key stages of evolution of the magma reservoir prior to eruption: long-term mush residence (**a**) and pre-eruptive remobilisation (**b**). Coloured circles correspond to locations of the magmatic clast samples. For most of the reservoir's lifetime (**a**), magma is stored at high but variable crystallinity depending on proximity to the recharge heat source. Most of the magma volume is stored as immobile, rigid crystal

framework (‘mush’, > ca. 50% crystals) below titanite saturation (T ttn ~ 730 °C). Locally, pools of evolved melt may form by extraction from the crystal framework. Where the amount of supplied heat is insufficient, magma solidifies to form the plutonic rind of the system. (**b**) In the last ca. 50 ky prior to eruption, an increase in recharge rate results in a gradual, large-scale decrease in crystallinity (to about 40–50%, i.e. eruptible state), which may facilitate homogenisation by overturn. The ultimately erupted material is a mixture of different environments within the magma reservoir, volumetrically dominated by the mush zone, with a minor proportion of extracted melts. (**c**) A schematic depiction of the temperature evolution of the KNT reservoir, with temperature cycling as a function of recharge. Individual clasts sample the same maturation history but differ in the time and mode of final cooling, from early solidification of some porphyry and plutonic lithologies to quenching upon eruption for the pumices.

References

Arzilli, F., Fabbrizio, A., Schmidt, M.W., Petrelli, M., Maimaiti, M., Dingwell, D.B., Paris, E., Burton, M., Carroll, M.R., 2018. The effect of diffusive re-equilibration time on trace element partitioning between alkali feldspar and trachytic melts. Chem. Geol. 495, 50-66.

Bachmann, O., Dungan, M.A., Lipman, P.W., 2002. The Fish Canyon magma body, San Juan volcanic field, Colorado: Rejuvenation and eruption of an upper-crustal batholith. J. Petrol. 43, 1469-1503.

Bachmann, O., Bergantz, G.W., 2003. Rejuvenation of the Fish Canyon magma body: A window into the evolution of large-volume silicic magma systems. Geology 31, 789-792.

Barboni, M., Boehnke, P., Schmitt, A.K., Harrison, T.M., Shane, P., Bouvier, A.-S., Baumgartner, L., 2016. Warm storage for arc magmas. Proc. Natl. Acad. Sci. USA 113, 13959-13964.

Burgisser, A., Bergantz, G.W., 2011. A rapid mechanism to remobilize and homogenize highly crystalline magma bodies. Nature 471, 212-215.

Chapin, C.E., Wilks, M., McIntosh, W.C., 2004. Space-time patterns of Late Cretaceous to present magmatism in New Mexico—Comparison with Andean volcanism and potential for future volcanism. New Mexico Bureau of Geology and Mineral Resources Bulletin 160, 13-40.

Cherniak, D.J., Watson, E.B., 2003. Diffusion in zircon. Rev. Mineral. Geochem. 53, 113-143.

Claiborne, L.L., Miller, C.F., Gualda, G.A., Carley, T.L., Covey, A.K., Wooden, J.L., Fleming, M.A., 2018. Zircon as Magma Monitor: Robust, Temperature-Dependent Partition Coefficients from Glass and Zircon Surface and Rim Measurements from Natural Systems, in: Moser, D.E., Corfu, F., Darling, J.R., Reddy, S.M., Tait, K. (Eds.), Microstructural Geochronology: Planetary Records Down to Atom Scale, Geophysical Monograph 232.

Coleman, D.S., Gray, W., Glazner, A.F., 2004. Rethinking the emplacement and evolution of zoned plutons: Geochronologic evidence for incremental assembly of the Tuolumne Intrusive Suite, California. Geology 32, 433.

Coney, P.J., Reynolds, S.J., 1977. Cordilleran Benioff Zones. Nature 270, 403-406.

Cooper, K.M., Kent, A.J.R., 2014. Rapid remobilization of magmatic crystals kept in cold storage. Nature 506, 480-483.
Cooper, K.M., 2015. Timescales of crustal magma reservoir processes: insights from U-series crystal ages. Geol. Soc. Spec. Publ. 422, 141-174.
Costa, F., 2008. Residence Times of Silicic Magmas Associated with Calderas, in: Gottsmann, J., Martí, J. (Eds.), Caldera Volcanism: Analysis, Modelling and Response: Developments in Volcanology Volume 10. Elsevier, Amsterdam, pp. 1-55.
Costa, F., Dohmen, R., Chakraborty, S., 2008. Time Scales of Magmatic Processes from Modeling the Zoning Patterns of Crystals. Rev. Mineral. Geochem. 69, 545-594.
Davis, J.M., Hawkesworth, C.J., 1993. The petrogenesis of 30–20 Ma basic and intermediate volcanics from the Mogollon-Datil Volcanic Field, New Mexico, USA. Contrib. Mineral. Petrol. 115, 165-183.
Elston, W.E., 1957. Geology and mineral resources of Dwyer quadrangle, Grant, Luna, and Sierra Counties, New Mexico. NM Bur. Mines Miner. Res. Bull. 38.
Elston, W.E., Seager, W.R., Clemons, R.E., 1975. Emory Cauldron, Black Range, New Mexico, source of the Kneeling Nun Tuff, in: Seager, W.R., Clemons, R.E., Callender, J.F. (Eds.), New Mexico Geological Society 26th Fall Field Conference Guidebook, pp. 283-292.
Elston, W.E., 1984. Mid-Tertiary ash flow tuff cauldrons, southwestern New Mexico. J. Geophys. Res. 89, 8733-8750.
Elston, W.E., 1989. Day 5: Field guide to the Emory caldera along NM-152 and in Tierra Blanca Canyon, in: Chapin, C.E., Zidek, J. (Eds.), Field excursions to volcanic terranes in the western United States, Volume I: Southern Rocky Mountain region, pp. 91-106.
Farmer, G.L., Bailley, T., Elkins-Tanton, L.T., 2007. Mantle source volumes and the origin of the mid-Tertiary ignimbrite flare-up in the southern Rocky Mountains, western US. Lithos 102, 279-294.
Ferry, J.M., Watson, E.B., 2007. New thermodynamic models and revised calibrations for the Ti-in-zircon and Zr-in-rutile thermometers. Contrib. Mineral. Petrol. 154, 429-437.
Flinders, A.F., Shelly, D.R., Dawson, P.B., Hill, D.P., Tripoli, B., Shen, Y., 2018. Seismic evidence for significant melt beneath the Long Valley Caldera, California, USA. Geology 46, 799-802.
Forni, F., Bachmann, O., Mollo, S., De Astis, G., Gelman, S.E., Ellis, B.S., 2016. The origin of a zoned ignimbrite: Insights into the Campanian Ignimbrite magma chamber (Campi Flegrei, Italy). Earth Planet. Sci. Lett. 449, 259-271.
Gelman, S.E., Gutiérrez, F.J., Bachmann, O., 2013. On the longevity of large upper crustal silicic magma reservoirs. Geology 41, 759-762.
Giles, D., 1965. Some aspects of the Kneeling Nun rhyolite tuff, in: Fitzsimmons, J.P., Balk, C.L. (Eds.), New Mexico Geological Society 16th Fall Field Conference Guidebook, pp. 164-166.
Giles, D.L., 1968. Ash-flow tuffs of the Cobre Mountains, Southern Arizona Guidebook III. Arizona Geological Society, pp. 289-291.
Gradstein, F., Ogg, J., Schmitz, M., Ogg, G., 2012. The Geologic Timescale 2012. Elsevier, Oxford.
Grimes, C.B., Wooden, J.L., Cheadle, M.J., John, B.E., 2015. "Fingerprinting" tectono-magmatic provenance using trace elements in igneous zircon. Contrib. Mineral. Petrol. 170.
Holland, T., Blundy, J., 1994. Non-ideal interactions in calcic amphiboles and their bearing on amphibole-plagioclase thermometry. Contrib. Mineral. Petrol. 116, 433-447.
Huber, C., Bachmann, O., Dufek, J., 2012. Crystal-poor versus crystal-rich ignimbrites: A competition between stirring and reactivation. Geology 40, 115-118.
Kaiser, J.F., de Silva, S., Schmitt, A.K., Economos, R., Sunagua, M., 2017. Million-year melt–presence in monotonous intermediate magma for a volcanic–plutonic assemblage in the Central Andes: Contrasting histories of crystal-rich and crystal-poor super-sized silicic magmas. Earth Planet. Sci. Lett. 457, 73-86.
Karakas, O., Degruyter, W., Bachmann, O., Dufek, J., 2017. Lifetime and size of shallow magma bodies controlled by crustal-scale magmatism. Nat. Geosci. 10, 446-450.
Keller, C.B., Schoene, B., Samperton, K.M., 2018. A stochastic sampling approach to zircon eruption age interpretation. Geochem. Persp. Let. 8, 31-35.
Kent, A.J.R., Cooper, K.M., 2017. How well do zircons record the thermal evolution of magmatic systems? Geology 46, 111-114.
Kiser, E., Levander, A., Zelt, C., Schmandt, B., Hansen, S.J.G., 2018. Focusing of melt near the top of the Mount St. Helens (USA) magma reservoir and its relationship to major volcanic eruptions. Geology 46, 775-778.
Kuellmer, F.J., 1954. Geologic section of the Black Range at Kingston, New Mexico. NM Bur. Mines Miner. Res. Bull. 33.
Kuiper, K.F., Deino, A., Hilgen, F.J., Krijgsman, W., Renne, P.R., Wijbrans, J.R., 2008. Synchronizing rock clocks of Earth history. Science 320, 500-504.
Lipman, P.W., Prostka, H.J., Christiansen, R.L., 1972. Cenozoic Volcanism and Plate-Tectonic Evolution of the Western United States. I. Early and Middle Cenozoic. Philos. T. Roy. Soc. A 271, 217-248.
Lipman, P.W., 2007. Incremental assembly and prolonged consolidation of Cordilleran magma chambers: Evidence from the Southern Rocky Mountain volcanic field. Geosphere 3, 42.

Marsh, B.D., 1981. On the crystallinity, probability of occurrence, and rheology of lava and magma. Contrib. Mineral. Petrol. 78, 85-98.

Mason, B.G., Pyle, D.M., Oppenheimer, C., 2004. The size and frequency of the largest explosive eruptions on Earth. Bull. Volcanol. 66, 735-748.

Matthews, N.E., Vazquez, J.A., Calvert, A.T., 2015. Age of the Lava Creek supereruption and magma chamber assembly at Yellowstone based on 40Ar/39Ar and U-Pb dating of sanidine and zircon crystals. Geochem. Geophys. Geosyst. 16, 2508-2528.

McDowell, F.W., McIntosh, W.C., 2012. Timing of intense magmatic episodes in the northern and central Sierra Madre Occidental, western Mexico. Geosphere 8, 1505.

McIntosh, W.C., Sutter, J.F., Chapin, C.E., Kedzie, L.L., 1990. High-precision 40Ar/39Ar sanidine geochronology of ignimbrites in the Mogollon-Datil volcanic field, southwestern New Mexico. Bull. Volcanol. 52, 584-601.

McIntosh, W.C., Chapin, C.E., Ratté, J.C., Sutter, J.F., 1992. Time-stratigraphic framework for the Eocene-Oligocene Mogollon-Datil volcanic field, southwest New Mexico. Geol. Soc. Am. Bull. 104, 851-871.

Melnik, O.E., Bindeman, I.N., 2018. Modeling of trace elemental zoning patterns in accessory minerals with emphasis on the origin of micrometer-scale oscillatory zoning in zircon. Am. Mineral. 103, 355-368.

Mutch, E.J.F., Blundy, J.D., Tattitch, B.C., Cooper, F.J., Brooker, R.A., 2016. An experimental study of amphibole stability in low-pressure granitic magmas and a revised Al-in-hornblende geobarometer. Contrib. Mineral. Petrol. 171, 85.

Putirka, K.D., 2008. Thermometers and barometers for volcanic systems. Rev. Mineral. Geochem. 69, 61-120.

Rivera, T.A., Schmitz, M.D., Crowley, J.L., Storey, M., 2014. Rapid magma evolution constrained by zircon petrochronology and 40Ar/39Ar sanidine ages for the Huckleberry Ridge Tuff, Yellowstone, USA. Geology 42, 643-646.

Samperton, K.M., Schoene, B., Cottle, J.M., Keller, C.B., Crowley, J.L., Schmitz, M.D., 2015. Magma emplacement, differentiation and cooling in the middle crust: Integrated zircon geochronological–geochemical constraints from the Bergell Intrusion, Central Alps. Chem. Geol. 417, 322-340.

Samperton, K.M., Bell, E.A., Barboni, M., Keller, C.B., Schoene, B., 2017. Zircon age-temperature-compositional spectra in plutonic rocks. Geology 45, 983-986.

Schaltegger, U., Brack, P., Ovtcharova, M., Peytcheva, I., Schoene, B., Stracke, A., Marocchi, M., Bargossi, G.M., 2009. Zircon and titanite recording 1.5 million years of magma accretion, crystallization and initial cooling in a composite pluton (southern Adamello batholith, northern Italy). Earth Planet. Sci. Lett. 286, 208-218.

Schmitz, M.D., Davydov, V.I., 2011. Quantitative radiometric and biostratigraphic calibration of the Pennsylvanian-Early Permian (Cisuralian) time scale and pan-Euramerican chronostratigraphic correlation. Geol. Soc. Am. Bull. 124, 549-577.

Schoene, B., Latkoczy, C., Schaltegger, U., Günther, D., 2010. A new method integrating high-precision U–Pb geochronology with zircon trace element analysis (U–Pb TIMS-TEA). Geochim. Cosmochim. Acta 74, 7144-7159.

Schoene, B., Schaltegger, U., Brack, P., Latkoczy, C., Stracke, A., Günther, D., 2012. Rates of magma differentiation and emplacement in a ballooning pluton recorded by U–Pb TIMS-TEA, Adamello batholith, Italy. Earth Planet. Sci. Lett. 355-356, 162-173.

Schoene, B., Samperton, K.M., Eddy, M.P., Keller, G., Adatte, T., Bowring, S.A., Khadri, S.F., Gertsch, B., 2015. U-Pb geochronology of the Deccan Traps and relation to the end-Cretaceous mass extinction. Science 347, 182-184.

Self, S., 2006. The effects and consequences of very large explosive volcanic eruptions. Philos. T. Roy. Soc. A 364, 2073-2097.

Stelten, M.E., Cooper, K.M., Vazquez, J.A., Reid, M.R., Barfod, G.H., Wimpenny, J., Yin, Q.-z., 2013. Magma mixing and the generation of isotopically juvenile silicic magma at Yellowstone caldera inferred from coupling 238U–230Th ages with trace elements and Hf and O isotopes in zircon and Pb isotopes in sanidine. Contrib. Mineral. Petrol. 166, 587-613.

Szymanowski, D., Wotzlaw, J.F., Ellis, B.S., Bachmann, O., Guillong, M., von Quadt, A., 2017. Protracted near-solidus storage and pre-eruptive rejuvenation of large magma reservoirs. Nat. Geosci. 10, 777-782.

Szymanowski, D., Fehr, M.A., Guillong, M., Coble, M.A., Wotzlaw, J.F., Nasdala, L., Ellis, B.S., Bachmann, O., Schönbächler, M., 2018. Isotope-dilution anchoring of zircon reference materials for accurate Ti-in-zircon thermometry. Chem. Geol. 481, 146-154.

Tierney, C.R., Schmitt, A.K., Lovera, O.M., de Silva, S.L., 2016. Voluminous plutonism during volcanic quiescence revealed by thermochemical modeling of zircon. Geology 44, 683-686.

Vazquez, J.A., Reid, M.R., 2004. Probing the accumulation history of the voluminous Toba magma. Science 305, 991-994.

Watson, E.B., 1996. Dissolution, growth and survival of zircons during crustal fusion: Kinetic principles, geological models and implications for isotopic inheritance. Trans. R. Soc. Edinburgh Earth Sci. 87, 43-56.

Wolff, J.A., Ellis, B.S., Ramos, F.C., Starkel, W.A., Boroughs, S., Olin, P.H., Bachmann, O., 2015. Remelting of cumulates as a process for producing chemical zoning in silicic tuffs: A comparison of cool, wet and hot, dry rhyolitic magma systems. Lithos 236–237, 275-286.

Wotzlaw, J.-F., Brack, P., Storck, J.-C., 2018. High-resolution stratigraphy and zircon U–Pb geochronology of the Middle Triassic Buchenstein Formation (Dolomites, northern Italy): precession-forcing of hemipelagic carbonate sedimentation and calibration of the Anisian–Ladinian boundary interval. J. Geol. Soc. London 175, 71-85.

Wotzlaw, J.F., Schaltegger, U., Frick, D.A., Dungan, M.A., Gerdes, A., Günther, D., 2013. Tracking the evolution of large-volume silicic magma reservoirs from assembly to supereruption. Geology 41, 867-870.

Figures
Click here to download Figure: Figures_KNT.pdf

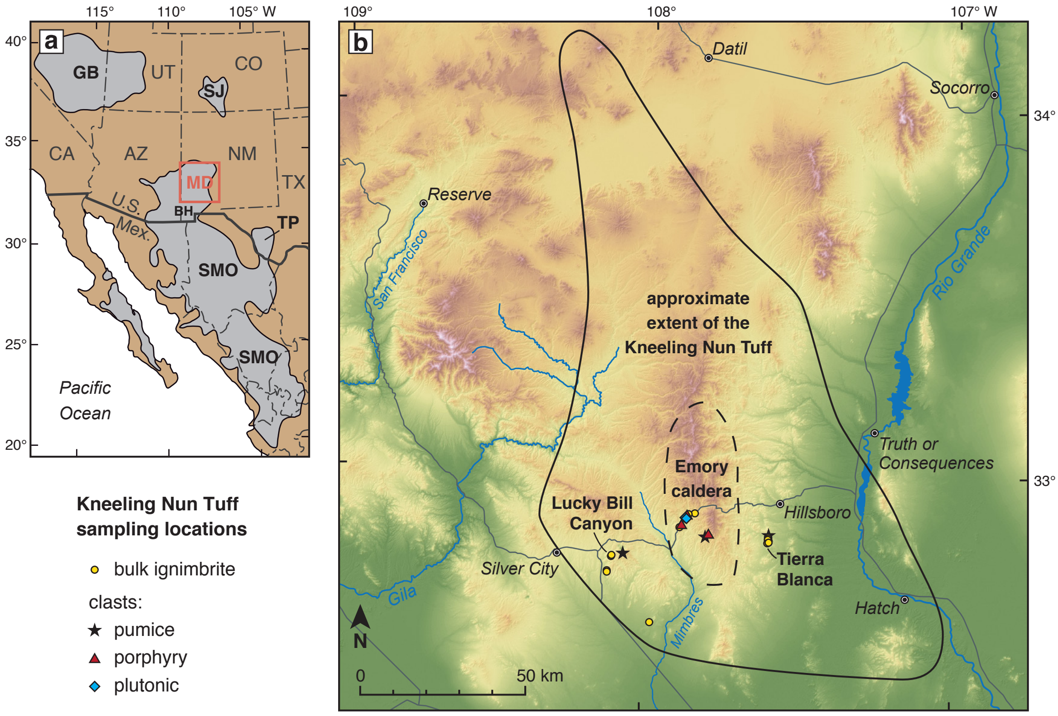

Fig. 1. Location of the study area and Kneeling Nun Tuff sampling sites. (**a**) Map of the distribution of Tertiary volcanic rocks in SW North America (modified from McDowell and McIntosh, 2012); SJ–San Juan/Southern Rocky Mountain volcanic field; MD–Mogollon–Datil; BH–Boot Heel; TP–Trans-Pecos; SMO–Sierra Madre Occidental; GB–Great Basin. (**b**) Location of the Emory caldera, source of the Kneeling Nun Tuff, within the Mogollon–Datil volcanic field in western New Mexico, with the approximate extent of the KNT ignimbrite sheet proposed by McIntosh et al. (1992) based on paleomagnetic and $^{40}Ar/^{39}Ar$ data of distal samples. Three key areas were targeted for sampling: western outflow sheet at Lucky Bill Canyon, Hurley and inside Chino Mine; intracaldera KNT along NM-152 west of Emory Pass; eastern outflow sheet immediately south of Tierra Blanca valley.

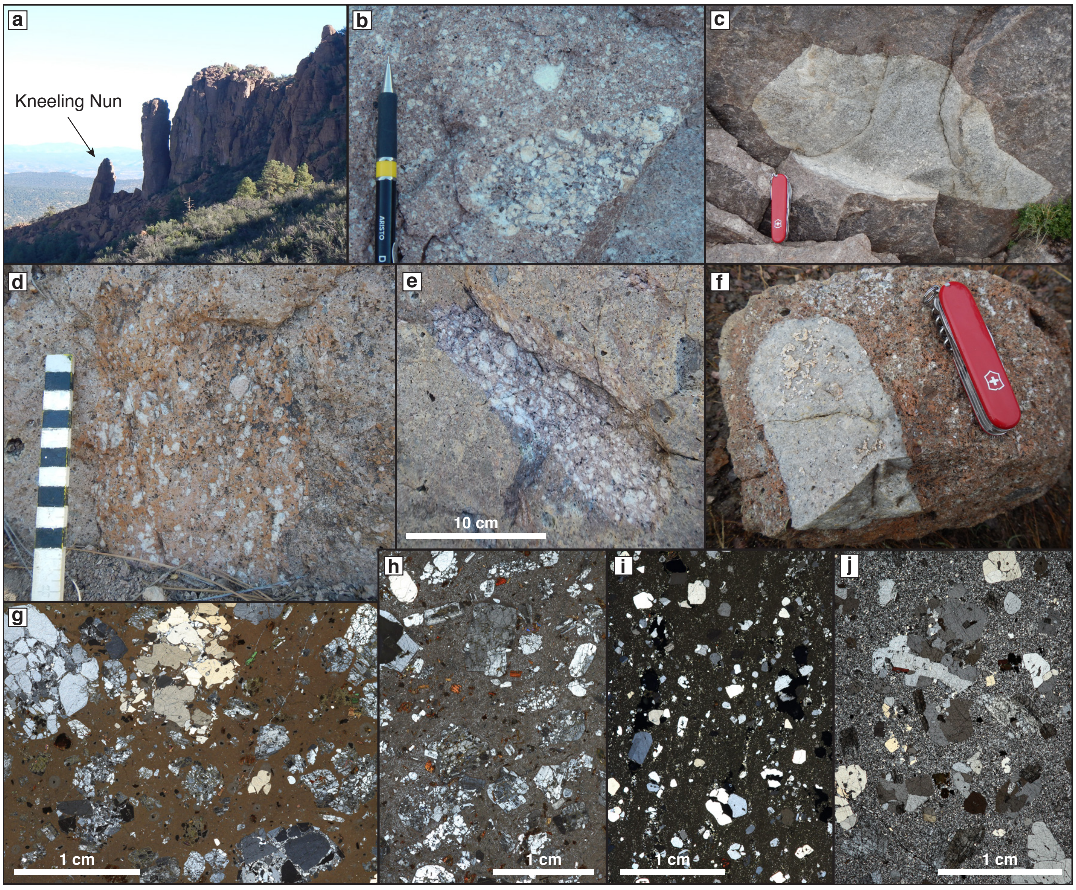

Fig. 2. Field appearance and microscopic textures of studied lithologies. (**a**) The eruptive unit's namesake, the Kneeling Nun landmark near Santa Rita, NM. (**b–f**) Field appearance of studied clasts including crystal-rich pumice (**b**), plutonic clasts (**c,f**) and porphyries (**d,e**). The field scale in d is marked every 1 cm. (**g–j**) Cross-polarised light thin section images of representative samples of a porphyry (1509A, **g**), a crystal-rich pumice (1525-2, **h**), an evolved quartz-rich pumice (1434, **i**) and a holocrystalline granitic clast (1421, **j**).

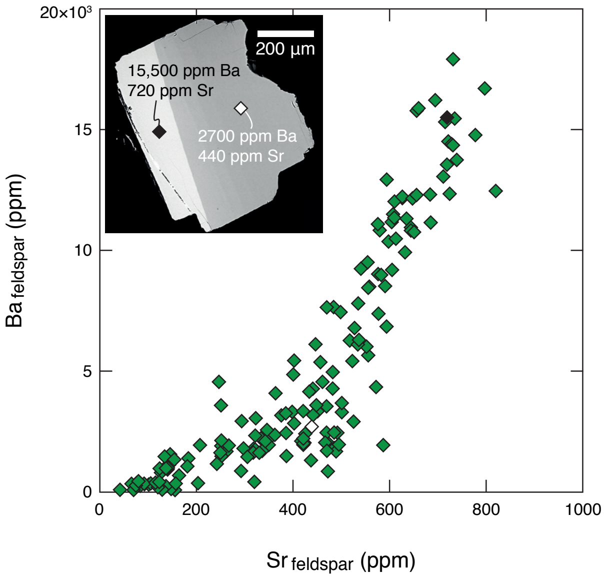

Fig. 3. Trace element (Ba, Sr) compositions of representative KNT sanidine, illustrating the magnitude of variations in compatible elements. Inset: a backscattered electron image of a sanidine crystal typical for late-erupted material (Table 1) with a prominent high-Ba rim.

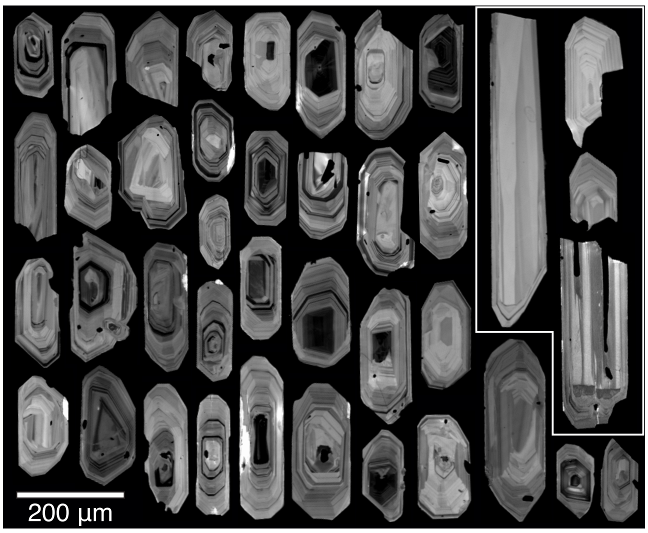

Fig. 4. Cathodoluminescence (CL) images of representative Kneeling Nun Tuff zircon crystals from samples 1402, 1416, 1509A, 1511, and 1525-2. Note the frequent truncations and complex zonation patterns. The white frame highlights CL-bright, simply zoned, REE-depleted crystals with $^{206}Pb/^{238}U$ dates between 35.352 and 35.305 Ma.

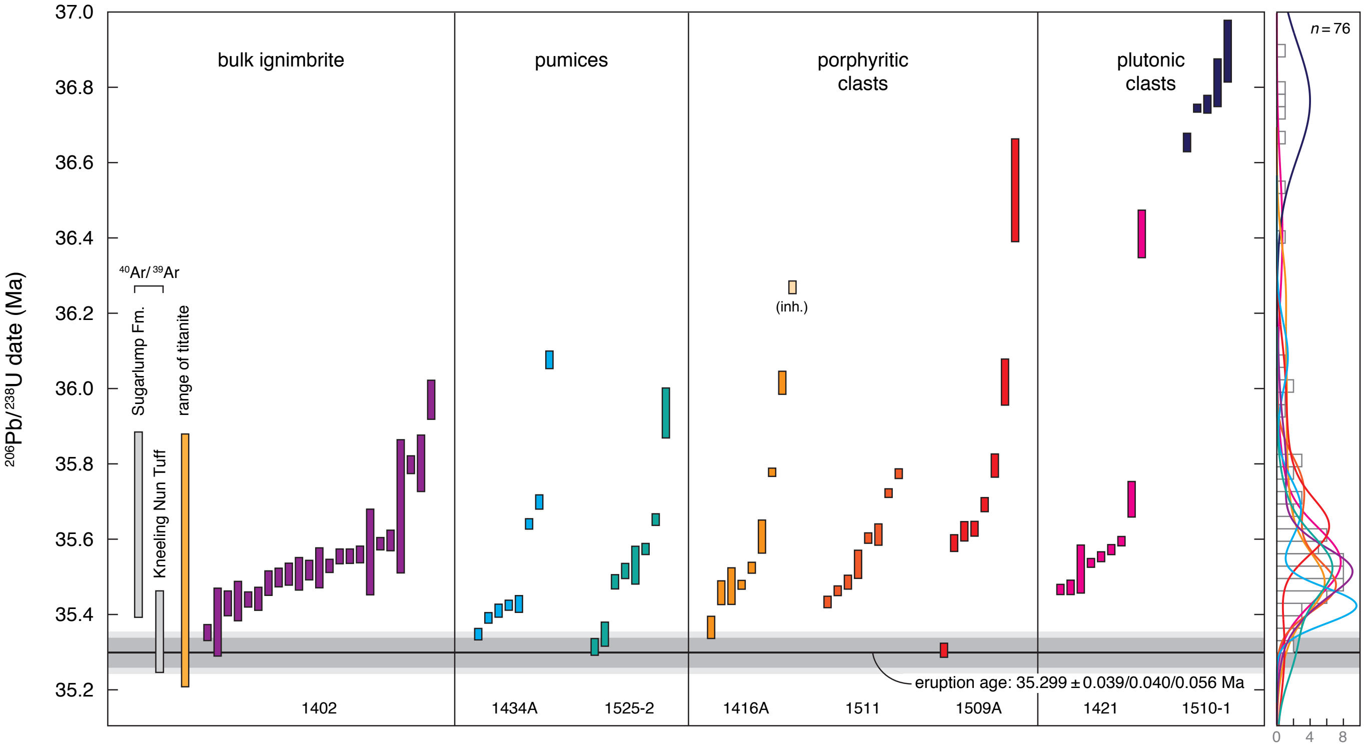

Fig. 5. Texturally resolved geochronology of the Kneeling Nun magmatic system. Coloured bars represent Th-corrected ID-TIMS $^{206}Pb/^{238}U$ dates of individual zircon crystals together with their 2σ uncertainty. Bulk-ignimbrite zircon and titanite data for sample 1402 is reproduced from Szymanowski et al. (2017). $^{40}Ar/^{39}Ar$ sanidine dates for KNT and uppermost Sugarlump tuffs (McIntosh et al., 1990) were recalculated to the calibration of Kuiper et al. (2008). The preferred eruption age is the Bayesian estimate following Keller et al. (2018) displayed with three uncertainty envelopes: internal only/with tracer calibration/with tracer and ^{238}U decay constant. Side panel: colour-coded kernel density plots illustrating the zircon age distribution of individual samples and a histogram of all zircon dates in this study.

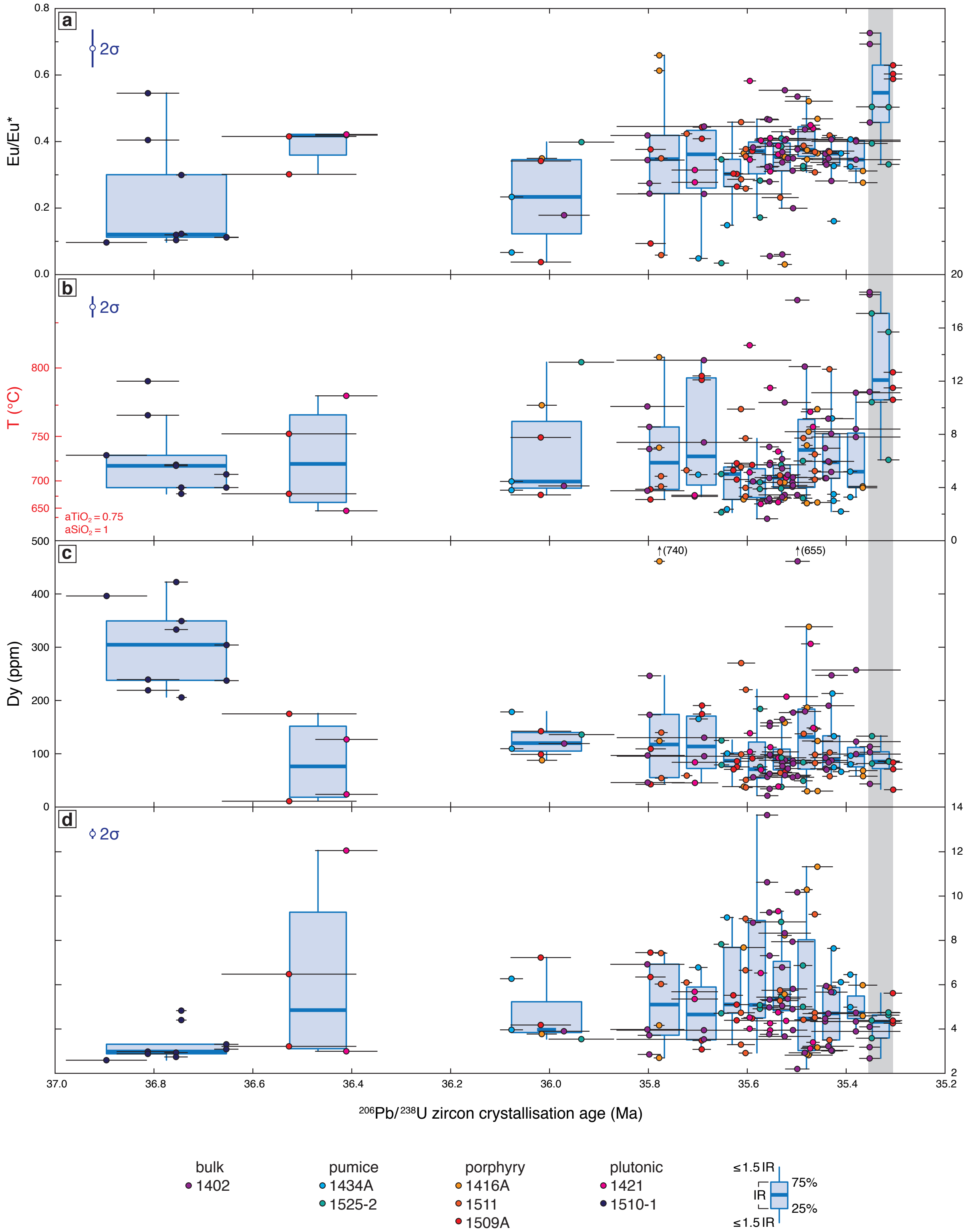

Fig. 6. Variability of selected trace elements in Kneeling Nun Tuff zircon through time. Each point represents one in situ LA-ICPMS analysis prior to ID-TIMS U–Pb dating of the bulk crystal; in cases where multiple spot analyses of a crystal are available, they are assigned the same crystallisation age. Note that the real crystallisation ages of the sampled spots may deviate from the assigned ones as bulk U–Pb dates are likely to be biased towards ages of rims and high-U zones. Box plots show medians, interquartile ranges (IR), and extreme values for bins of 50 ky (7 youngest bins) or more (dates > 35.655 Ma). T-tests for Eu/Eu* (**a**) and Ti (**b**) reveal that compositions of zircon in the youngest bin (50 ky prior to eruption, grey shaded area) are statistically distinct from the compositions of older crystals at high significance level ($p < 0.01$). These younger crystals further show significantly lower variance with respect to Dy and Yb/Dy. Typical uncertainties are based on counting statistics for element ratios (Yb/Dy, Eu/Eu*) or counting statistics and the composition of primary reference materials for Ti and Dy. For Dy the error bar is smaller than symbol size. Ti was either analysed relative to reference zircon GZ7 (Szymanowski et al., 2018) for clast-hosted zircon or recalculated to match the same calibration (via zircon 91500) for previously analysed zircon from bulk sample 1402. Ti-in-zircon temperature estimates use the model of Ferry and Watson (2007).

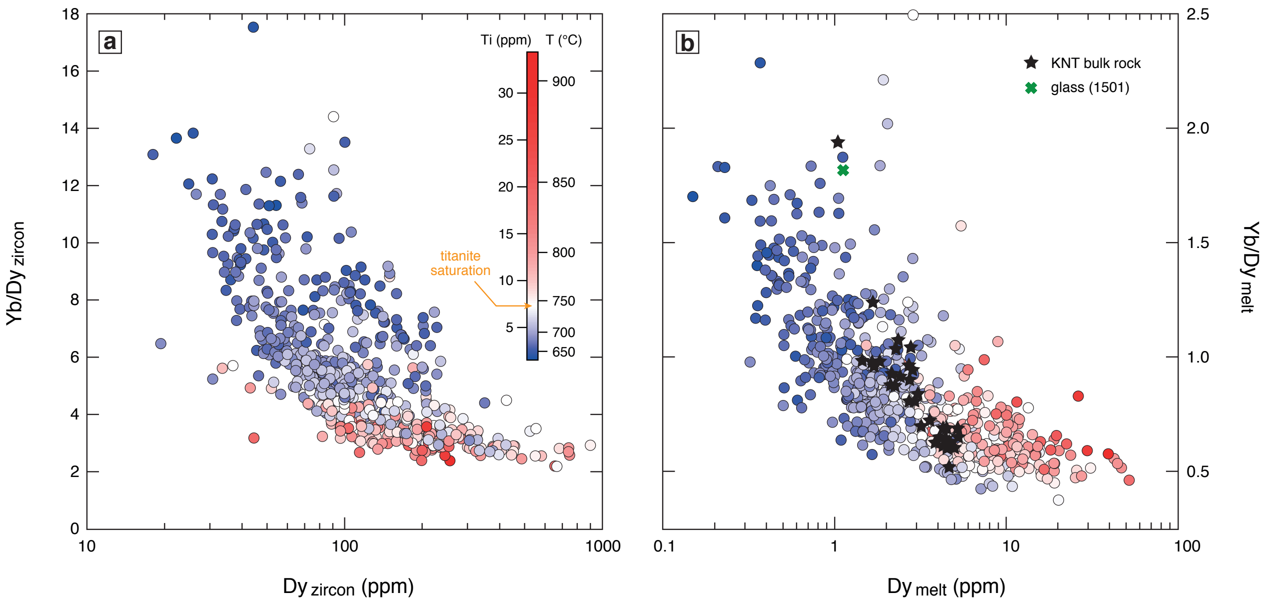

Fig. 7. Trace elements in zircon and their corresponding melts, colour-coded for Ti content in zircon. (**a**) Results of LA-ICPMS measurements of KNT zircon across all dated samples. (**b**) Melts in equilibrium with individual measured zircon compositions, calculated using power-law fits between Ti and zircon–melt partition coefficients (Claiborne et al., 2018). Titanite saturation temperature is the average Zr-in-titanite temperature of Szymanowski et al. (2017) adjusted for pressure of 2.2 kbar.

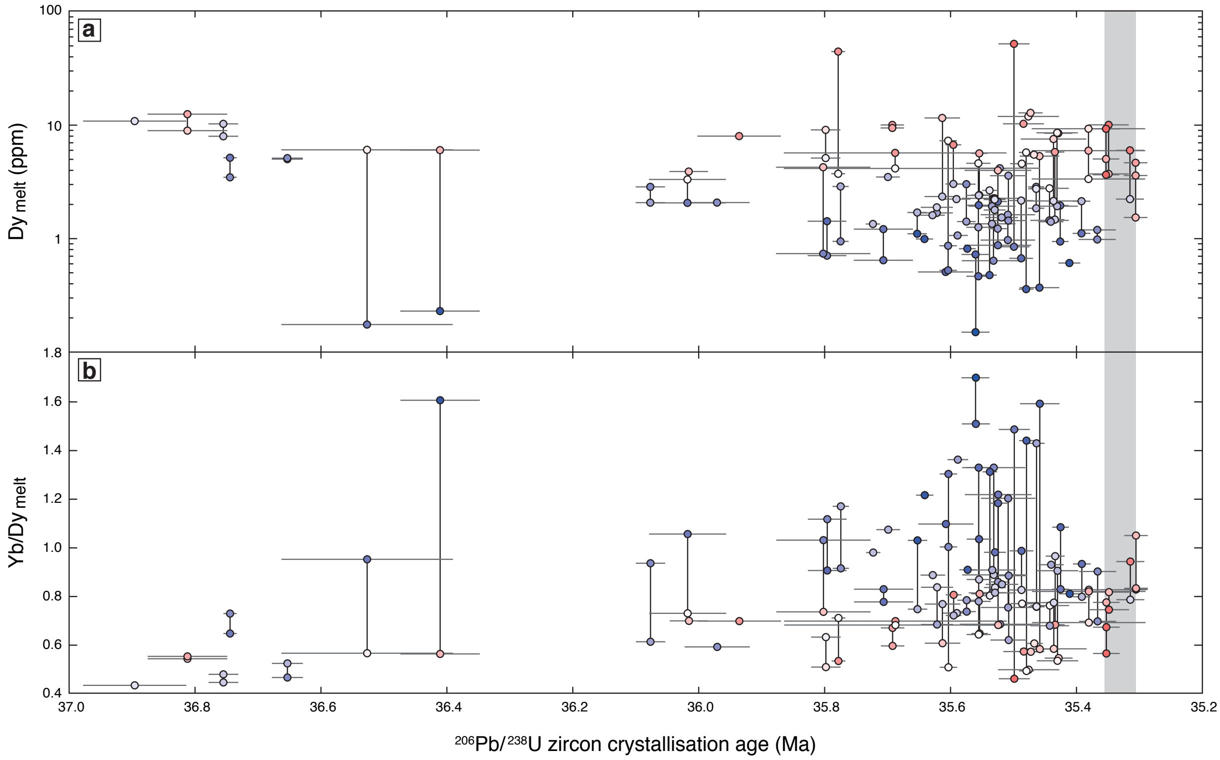

Fig. 8. Composition of reconstructed Kneeling Nun Tuff melts through time. Each point corresponds to a datum in Fig. 6. The time coordinate is identical to that of the corresponding whole-zircon crystallisation age, while the composition is recalculated from the respective in situ zircon analysis using the model of Claiborne et al. (2018) as in Fig. 7. In cases of multiple compositions assigned to the same age, the points are connected with a vertical line.

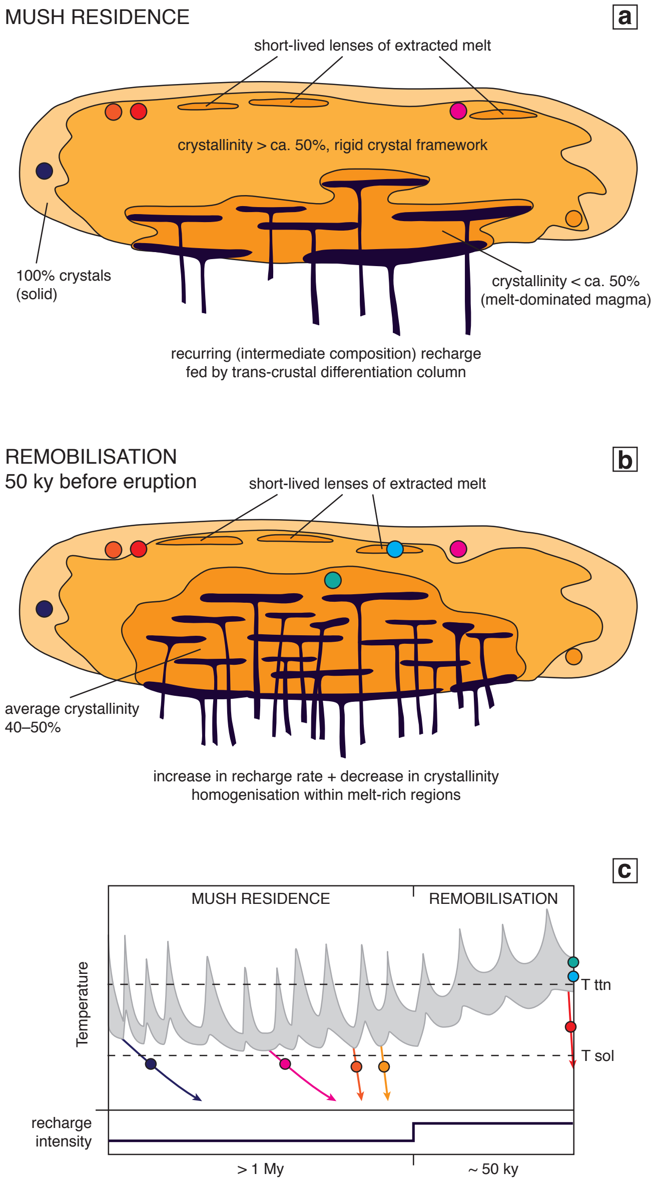

Fig. 9. Conceptual model of the storage and remobilisation of the Kneeling Nun magmatic system. (**a–b**) Two key stages of evolution of the magma reservoir prior to eruption: long-term mush residence (**a**) and pre-eruptive remobilisation (**b**). Coloured circles correspond to locations of the magmatic clast samples. For most of the reservoir's lifetime (**a**), magma is stored at high but variable crystallinity depending on proximity to the recharge heat source. Most of the magma volume is stored as immobile, rigid crystal framework ('mush', > ca. 50% crystals) below titanite saturation (T ttn ~ 730 °C). Locally, pools of evolved melt may form by extraction from the crystal framework. Where the amount of supplied heat is insufficient, magma solidifies to form the plutonic rind of the system. (**b**) In the last ca. 50 ky prior to eruption, an increase in recharge rate results in a gradual, large-scale decrease in crystallinity (to about 40–50%, i.e. eruptible state), which may facilitate homogenisation by overturn. The ultimately erupted material is a mixture of different environments within the magma reservoir, volumetrically dominated by the mush zone, with a minor proportion of extracted melts. (**c**) A schematic depiction of the temperature evolution of the KNT reservoir, with temperature cycling as a function of recharge. Individual clasts sample the same maturation history but differ in the time and mode of final cooling, from early solidification of some porphyry and plutonic lithologies to quenching upon eruption for the pumices.

Table 1
Click here to download Table: Table 1.docx

Table 1

Summary of crystallinities, compositions and intensive parameters calculated for key samples of Kneeling Nun Tuff and its magmatic clasts.

Sample	crystallinity [%] [a]	SiO_2 [wt%] [b]	plagioclase An [c]	sanidine Or [c]	high-Ba rims	two-feldspar T [°C] [cd]	amphibole–plagioclase T [°C] [e]	amphibole P [kbar] [fg]
bulk ignimbrite								
1519	11		13–16	69–71		640–689		
1520	58	76.9	13–23	63–65		697–762		
1521	32	72.9	14–27	62–65		718–785		
1522	49	69.0	20–28	61–64	x	767–823	744–803	2.21 ± 0.13
1402	46	69.5	21–28	61–66	x	729–822	746–801	2.21 ± 0.09
1523	55	67.1	21–27	61–64	x	765–833		
1428	32	75.8	11–23	61–65		675–763		
1430	48	75.1	19–23	62–65	x	747–777		
1435	44	75.7	20–23	59–64	x	722–810		
pumices								
1434A	26	77.1	14–19	62–65		700–728		
1525-2	46	70.3	20–27	62–64	x	757–849	757–810	2.19 ± 0.09
porphyrytic clasts								
1416A	56	73.8	18–24	64–68		729–780		
1509A	60	67.9	20–27	65–69	x	709–800	754–808	2.25 ± 0.16
1511	62	69.0	22–26	66–68	x	727–797	761–800	2.22 ± 0.09
plutonic clasts								
1421	100	75.6	15–22	61–63		695–740		
1510	100	77.0	16–19	61–62		684–750		

[a] crystallinity determined by point counting
[b] SiO_2 from XRF analyses, all major elements normalised to 100% on anhydrous basis
[c] excluding outliers as defined in Supplementary Fig. 4
[d] equation 27b of Putirka (2008)
[e] thermometer B of Holland and Blundy (1994)
[f] Mutch et al. (2016)
[g] reported uncertainty (1s) is a function of the scatter of Al tot in amphibole; the uncertainty of the thermometer calibration is ca. 0.4 kbar